Indonesian Physical Review
Volume 09 Issue 03, September 2026
P-ISSN: 2615-1278, E-ISSN: 2614-7904

Investigation of the Structural, Morphological, and Magnetic Properties of Barium Hexaferrite/Titania Nanocomposite

Mahmiyah[1], Suneyna Rawat[2,3], Nur Hanifah[1], Arif Hidayat[1*], Ahmad Taufiq[1]
[1] *Department of Physics, Faculty of Mathematics and Natural Science, Universitas Negeri Malang, Indonesia*
[2] *Centre for Solar Cells and Renewable Energy, Sharda University, Greater Noida, India*
[3] *Department of Physics, Sharda University, Greater Noida, India*

Corresponding Author's E-mail: arif.hidayat.fmipa@um.ac.id

Article Info

Article info:
Received: 15-05-2026
Revised: 24-08-2026
Accepted: 15-09-2026

Keywords:
Barium hexaferrite/titania; Ferrimagnetic; coprecipitation; sol–gel; wet mixing method

How To Cite:
Mahmiyah, S. Rawat, N. Hanifah, A. Hidayat, A. Taufiq, "Investigation of the Structural, Morphological, and Magnetic Properties of Barium Hexaferrite/Titania Nanocomposite", Indonesian Physical Review, vol. 9, no. 3, p 612-622, 2026.

DOI:
https://doi.org/10.29303/ipr.v9i3.692.

Abstract

Currently, demand for magnetic materials across various industrial sectors continues to grow. Among hard magnetic ferrites, barium hexaferrite is widely used due to its ability to retain magnetization after removal of the external magnetic field. Despite these advantages, its relatively high density and tendency to agglomerate can limit its use in certain applications. Therefore, titania was incorporated as a complementary phase to modify the properties of barium hexaferrite. This study presents a simple and modular approach for preparing a barium hexaferrite/titania nanocomposite through separate coprecipitation and sol–gel routes, followed by wet mixing of 0.6 g of barium hexaferrite and 0.4 g of titania. The resulting nanocomposite was characterized using XRD, SEM-EDX mapping, FTIR, and VSM. The XRD pattern revealed the formation of barium hexaferrite and anatase titania phases, with crystallite sizes of 62.12 and 15.26 nm, respectively, along with hematite and barium carbonate impurity phases. The FTIR spectrum showed characteristic bands associated with Ba–O, Fe–O, Ti–O, C–O, and O–H bonds. SEM-EDX mapping analysis revealed a dense and aggregated morphology with relatively uniform surface topography, containing Ba, Fe, Ti, and O. The VSM hysteresis curve demonstrated ferrimagnetic behavior, with M_s, M_r, and H_c values of 18.86 emu/g, 7.88 emu/g, and 4663 Oe, respectively.

Introduction

Currently, the industrial need for magnetic materials is increasing, especially hard ferrite magnetics [1,2]. The main advantage of hard magnetic materials lies in their natural properties, which enable them to retain magnetization for longer even after the external field is removed [3]. One of the popular hard magnetics being researched is Barium hexaferrite. Barium hexaferrite is a hard magnetic material with high saturation magnetization, high crystal anisotropy, good chemical stability, high Curie temperature, and corrosion resistance [4–8].

With these characteristics, barium hexaferrite is widely used in the military sector as an electromagnetic wave absorber because its high permeability and high magnetic saturation minimize impedance mismatch, thereby increasing absorption capability [9,10]. Barium hexaferrite is also used in the automotive industry as a permanent magnet in electric motors and sensors because of its high coercivity and chemical stability [11]. Barium hexaferrite can be used as a recording medium and magnet in television because of its high Curie temperature [12,13]. In addition, Barium hexaferrite has a relatively small bandgap, so it can absorb some direct sunlight irradiation [14,15].

However, despite the advantages of barium hexaferrite, certain properties, such as high density and susceptibility to agglomeration, limit its use in certain applications. Therefore, modifications to its structure, morphology, or magnetic properties are required and can be achieved through temperature changes, doping, or combining it with other materials to achieve optimal characteristics. One of the excellent materials to combine with barium hexaferrite is titania. Titania is a semiconductor that has high dielectric, high chemical stability, high photosensitivity, is easy to synthesize, is non-toxic, has a large surface area, has a wide band gap, and acts as an anti-corrosive material [16–19]. Titania has been reported to exhibit dielectric and photocatalytic properties, making it a suitable counterpart to barium hexaferrite. Its tunable dielectric constant can help balance the magnetic response of barium hexaferrite for electromagnetic absorber applications [20,21], while its ability to promote electron–hole generation and reactive species formation contributes to photocatalytic activity [22,23]. Therefore, combining barium hexaferrite with titania provides complementary characteristics that may be relevant to various applications.

Accordingly, various synthesis strategies have been explored to integrate barium hexaferrite and titania. The use of different synthesis methods, temperatures, and phase ratios can affect the resulting crystal structure, morphology, and magnetic properties of the nanocomposites. For example, barium hexaferrite platelets have been prepared through a separate synthesis route and subsequently combined with titania with controlled crystal facets under controlled suspension conditions, resulting in hexagonal-shaped microplate facets [24]. Another study employed mechanical activation and subsequent calcination to prepare barium hexaferrite, then mixed it with titania at a 70:30 ratio and further sintered the mixture. The nanocomposite exhibited a slightly agglomerated morphology, accompanied by a decrease in magnetization after Ni incorporation [25]. More recently, barium hexaferrite has been synthesized via microwave and sol–gel autocombustion methods, followed by the formation of titania from titanium (IV) isopropoxide in the presence of preformed barium hexaferrite, and subsequent calcination. The microwave-assisted route produced nanoplate-shaped particles, whereas the sol–gel method yielded more sphere-like particles and was accompanied by the formation of impurity phases at a calcination temperature of 700 °C [26]. A similar approach has been reported in which titania was formed through a sol–gel process in the presence of barium hexaferrite at a 50:50 ratio, followed by additional thermal treatment to obtain the nanocomposite. The resulting material displayed an agglomerated morphology, along with moderate magnetization [27].

In this study, a modular preparation route was employed, in which barium hexaferrite and titania were synthesized independently via coprecipitation and sol–gel methods, respectively, and then combined by wet mixing. Unlike previously reported approaches that involve forming titania in the presence of barium hexaferrite, mechanical activation, or additional thermal treatment after composite formation, the present method combines two preformed

phases after their individual synthesis. This separation allows the preparation conditions for barium hexaferrite and titania to be controlled independently while avoiding the need for additional high-temperature treatment after their combination. The resulting barium hexaferrite/titania composite was investigated for its structural characteristics, functional groups, morphology, elemental distribution, and magnetic properties. This provides a clearer understanding of the properties that can be obtained when preformed barium hexaferrite and titania are combined through a simple post-synthesis mixing route.

Experimental Method

This research used materials in the form of iron (III) nitrate nonahydrate ($Fe(NO_3)_3 \cdot 9H_2O$), barium nitrate ($Ba(NO_3)_2$), sodium hydroxide (NaOH), nitric acid (HNO_3), isopropanol, glacial acetic acid, titanium (IV) isopropoxide (TTIP), and deionized water. Barium hexaferrite was synthesized via the coprecipitation method by mixing $Fe(NO_3)_3 \cdot 9H_2O$ and $Ba(NO_3)_2$ at a molar ratio of 12:1 in DI water, with constant stirring at 50°C. Then titrated with 3M NaOH to pH 12. Next, the solution was washed with 0.01M HNO_3 until the pH was neutral. The precipitate was dried at 100°C for 24 hours, then calcined at 1000°C for 5 hours. The formation of barium hexaferrite proceeds according to Equation (1).

$$Ba(NO_3)_2 + 12(Fe(NO_3)_3 \cdot 9H_2O) + 38NaOH \xrightarrow{\Delta} BaFe_{12}O_{19} + 38NaNO_3 + 127H_2O \quad (1)$$

Titania nanoparticles were synthesized via the sol–gel method by reacting isopropanol and glacial acetic acid with constant stirring for 30 minutes. Then, TTIP was added gradually to the mixture, followed by the addition of deionized water. The formed gel is then dried at 100°C for 2 hours, followed by calcination at 350°C for 3 hours. To form the barium hexaferrite/titania nanocomposite, 0.4 g of titania was mixed with 0.6 g of barium hexaferrite, which had been dispersed in 25 ml of deionized water, and the mixture was stirred continuously until homogeneous. Next, the barium hexaferrite/titania nanocomposite precipitate was dried at 100 °C for 60 minutes.

The barium hexaferrite/titania nanocomposite was identified through X-ray Diffraction (XRD) using an X'Pert Pro diffractometer with Cu-Kα radiation (λ = 1.54060 Å), and then further analysis was carried out using the Rietveld method to determine the lattice parameters and crystallite size. Next, a Fourier Transform Infra-Red (FTIR) was performed using the Shimadzu IR Prestige-21 instrument to identify functional groups and chemical bonds formed on the surface of the nanocomposite. Meanwhile, to evaluate the morphology and elemental composition of the nanocomposites, Scanning Electron Microscopy–Energy-Dispersive X-ray (SEM–EDX) mapping was performed using the FEI Inspect-S50 instrument. Furthermore, to determine the magnetic behavior of the nanocomposites, Vibrating-Sample Magnetometer (VSM) testing was conducted using a Quantum Design PPMS® VersaLab™ Cryogen-free 3T device.

Result and Discussion

The diffraction pattern of the barium hexaferrite/titania nanocomposite in the range 2θ = 20–80° is presented in Figure 1. The formation of the barium hexaferrite phase is confirmed by the peaks observed at 2θ = 30.98° (110), 32.33° (017), 34.13° (114), 35.74° (110), 37.19° (013), 38.03° (025), 40.48° (151), 42.55° (026), 50.0° (122), 54.14° (014), 55.22° (214), 56.65° (133), and 63.18° (153). Furthermore, Rietveld refinement analysis using the AMCSD database No. 0010651 revealed that barium hexaferrite has space group P63/mmc and lattice parameters a = b =

5.884 Å and c = 23.181 Å, with a hexagonal structure [28,29]. However, the XRD pattern also revealed the presence of impurity phases. The peaks observed at 2θ = 49.59° (222) and 64.16° (030) were assigned to hematite based on AMCSD No. 0017806, while the peak at 2θ = 33.27° (104) was attributed to barium carbonate according to AMCSD No. 0008422 [30–32]. Rietveld refinement further indicated that hematite and barium carbonate accounted for 15.58% and 1.01% of the total phase composition, respectively [30–32]. The formation of these minor impurity phases may be associated with the calcination conditions, particularly the calcination temperature and duration, and with the possible involvement of carbonate species during thermal treatment, as reported in previous studies [26,33,34]. As a result, the diffusion of Ba^{2+} and Fe^{3+} ions is limited, leading to hematite as a notable secondary phase [35,36]. Moreover, the peaks formed at 2θ = 25.36° (011), 38.24° (004), 48.13° (020), 54.09° (015), 55.01° (121), and 63.04° (024) indicate the presence of titania anatase (space group I41/AMD) according to the AMCSD database No.0019093. Titania had lattice parameters $a = b$ = 3.784 Å and c = 9.471 Å, consistent with a previous study [37]. The Rietveld refinement was also used to estimate the crystallite sizes, which were further corroborated by calculations using the Debye–Scherrer method (Equation 2), as given below.

$$D = \frac{k\lambda}{\beta cos\theta} \tag{2}$$

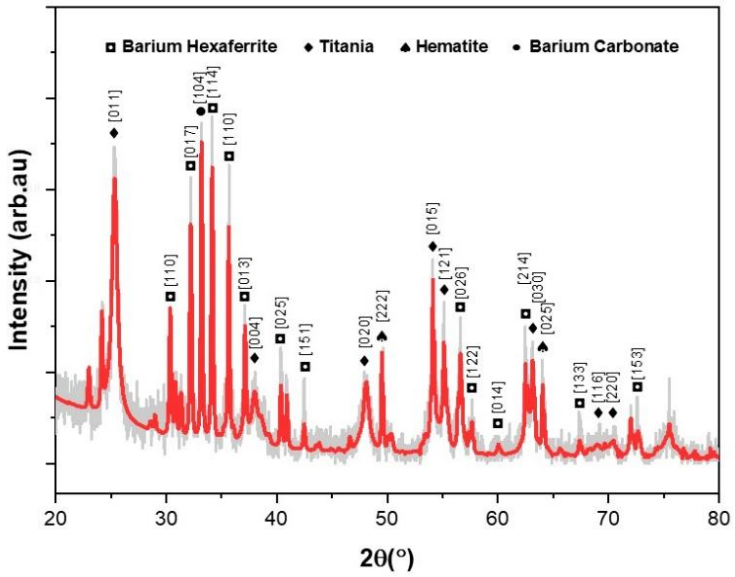

Figure 1. XRD pattern of barium hexaferrite/titania nanocomposite.

where D is the crystallite size (nm), k is a constant (0.9), λ is the Cu-Kα wavelength (1.5406 Å), β is the full width at half maximum (FWHM) value (rad), and θ is the Bragg angle. The crystallite sizes calculated using the Debye–Scherrer equation were consistent with those obtained from Rietveld refinement. The Rietveld analysis yielded crystallite sizes of 62.12 nm for barium hexaferrite and 15.26 nm for titania, while the Debye–Scherrer calculation yielded 61.68 and 14.78 nm, respectively, based on full width at half maximum (FWHM) values of approximately 0.1406° and 0.575° for the main diffraction peaks of barium hexaferrite and titania, respectively. Moreover, the refinement results yielded χ^2, Rp, Rwp, and GOF values of

1.24, 19.34, 26.88, and 1.73, respectively, indicating a reasonable agreement between the observed and calculated XRD patterns.

Furthermore, the FTIR analysis results at wavenumbers 400–4000 cm^{-1} are shown in Figure 2. The obtained FTIR spectrum revealed the presence of Fe–O vibrations at wave numbers 440 cm^{-1}, in accordance with previous research, which stated the existence of Fe–O bonds at wave numbers 420–600 cm^{-1} [38]. Apart from Fe–O vibrations, the presence of Ba–O vibrations in the 894 cm^{-1} area also confirmed the formation of the barium hexaferrite phase, in accordance with findings in previous studies [39,40]. The FTIR spectrum also showed the presence of absorption characteristics at a wave number of 702 cm^{-1}, which indicates the formation of Ti–O bonds in the nanocomposite [41]. The band at 1338 cm^{-1} is consistent with the symmetric C–O vibrations reported by Ismail et al., suggesting a possible contribution from the barium carbonate phase identified by XRD [42]. Furthermore, O–H bond stretching was observed in the area 3200–3600 cm^{-1}, confirming the adsorption process of water molecules on the surface of the barium hexaferrite/titania nanocomposite [27,43].

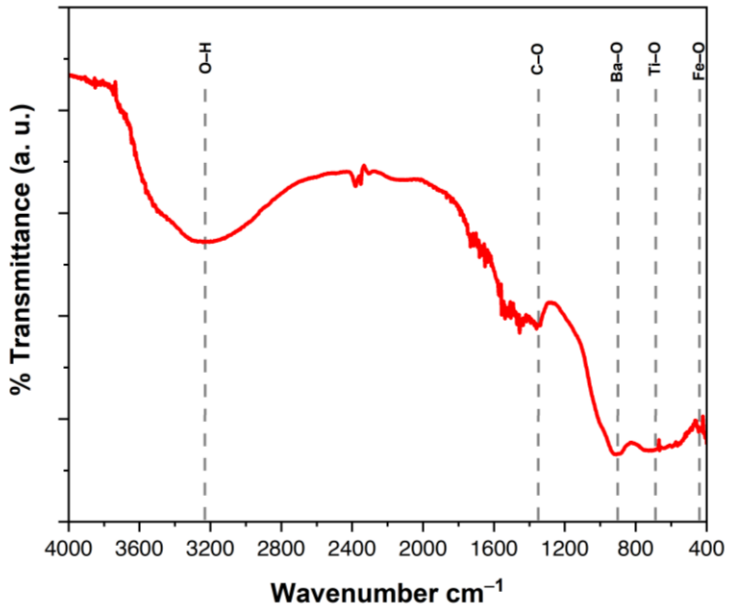

Figure 2. FTIR spectrum of barium hexaferrite/titania nanocomposite.

The morphology, EDX spectrum, and elemental mapping of the barium hexaferrite/titania nanocomposite are presented in Figure 3. Figure 3a shows that the barium hexaferrite/titania nanocomposite exhibits a relatively dense morphology with a uniform surface topography and well-dispersed particles. The particles appear to be distributed without pronounced localized agglomeration, suggesting a relatively homogeneous microstructure with a particle size of approximately 59.10 nm [24]. This morphological observation is supported by the EDX spectrum (Figure 3b), which confirms the presence of Ba, Fe, Ti, and O as the principal constituent elements of the nanocomposite. Furthermore, the SEM-EDX elemental mapping presented in Figure 3c demonstrates a relatively homogeneous spatial distribution of these elements across the analyzed area, with no apparent regions of significant elemental enrichment or segregation. The uniform distribution of the constituent elements indicates that the separately synthesized barium hexaferrite and titania phases were effectively dispersed

during mixing, resulting in a relatively uniform nanocomposite structure. Such a uniform morphology can facilitate close contact between the barium hexaferrite and titania phases, thereby enhancing interactions between the constituent phases and the resulting functional properties of the nanocomposite [44].

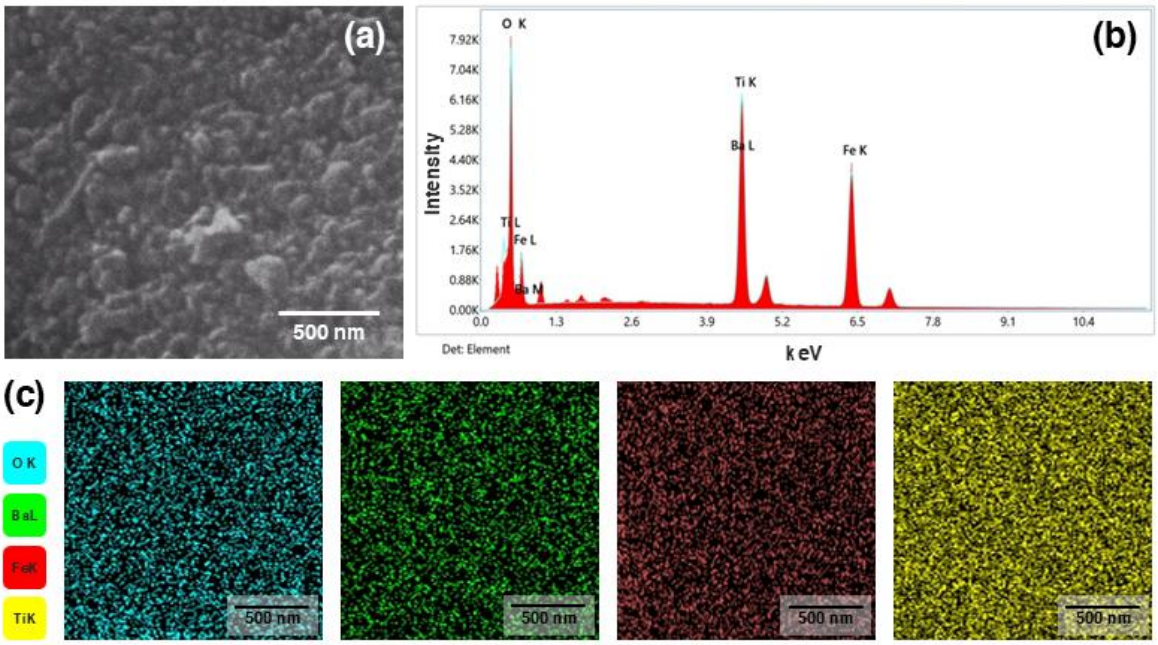

Figure 3. (a) Morphology, (b) EDX spectrum, and (c) Elemental mapping of barium hexaferrite/titania nanocomposite.

Figure 4 shows the hysteresis curve of the barium hexaferrite/titania nanocomposite obtained from VSM measurement. The curve exhibits predominantly ferrimagnetic behavior, which is an intrinsic characteristic of barium hexaferrite [25,45]. This is consistent with previous studies reporting saturation magnetization (M_s) values of approximately 38.86–55.81 emu/g for barium hexaferrite [46–48]. However, the incorporation of non-magnetic titania, together with the presence of hematite and barium carbonate impurity phases, tends to reduce the M_s value of the resulting nanocomposite to 18.86 emu/g, with remanent magnetization (M_r) and coercivity (H_c) values of 7.88 emu/g and 4663 Oe, respectively. Despite the reduced magnetization, the nanocomposite retains its ferrimagnetic behavior, reflecting the combined contribution of its constituent phases. These magnetic characteristics suggest that the barium hexaferrite/titania nanocomposite may be relevant to various functional applications, including photocatalysis, electromagnetic wave absorption, and other related applications, as reported in previous studies [24,25,49]. However, further application-specific investigations are required to evaluate its actual performance in these areas.

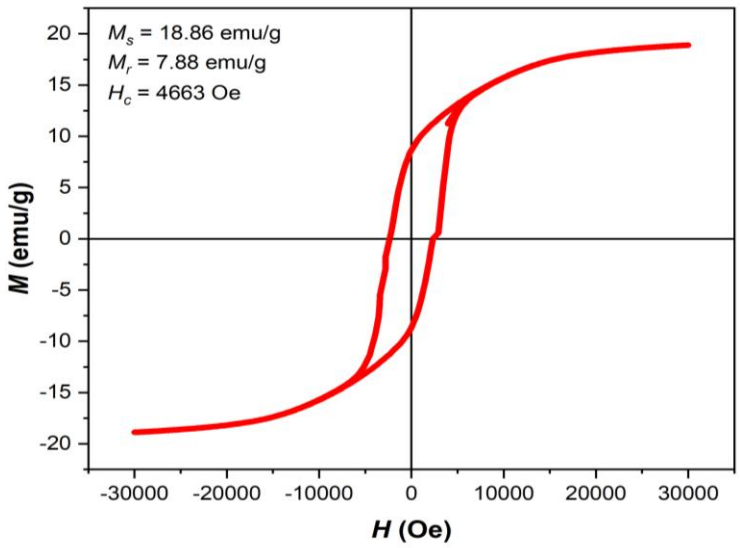

Figure 4. Hysteresis curve of barium hexaferrite/titania nanocomposite.

Conclusion

Barium hexaferrite/titania nanocomposite was prepared through separate coprecipitation and sol–gel routes, followed by wet mixing of the synthesized phases. XRD analysis confirmed the formation of barium hexaferrite and anatase titania, with Rietveld-refined crystallite sizes of 62.12 and 15.26 nm, respectively. Hematite and barium carbonate were also identified as impurity phases, with phase fractions of 15.58% and 1.01%, respectively. The FTIR spectrum showed characteristic Ba–O, Fe–O, Ti–O, C–O, and O–H vibrations associated with the constituent phases. SEM analysis revealed a relatively uniform surface morphology, while EDX and elemental mapping confirmed the presence and relatively homogeneous distribution of Ba, Fe, Ti, and O throughout the analyzed area. The nanocomposite exhibited ferrimagnetic behavior, with M_s, M_r, and H_c values of 18.86 emu/g, 7.88 emu/g, and 4663 Oe, respectively. Overall, the separate synthesis and subsequent wet-mixing route provides a simple and modular approach for combining barium hexaferrite and titania, allowing the synthesis conditions of each component to be controlled independently. The resulting structural, morphological, and magnetic characteristics provide a basis for further investigation of barium hexaferrite/titania nanocomposites for potential multifunctional applications.

Acknowledgment

This work was financially supported by Universitas Negeri Malang (UM) through research funding from the DPPM scheme, contract number 2.6.152/UN32.14.1/LT/2025.

References

[1] C. De Julian Fernandez, C. Sangregorio, J. De La Figuera, B. Belec, D. Makovec, and A. Quesada, "Topical Review: Progress and Prospects of Hard Hexaferrites for Permanent Magnet Applications," *J. Phys. Appl. Phys.*, vol. 54, p. 153001, Dec. 2020.

[2] J. MacDougall, H. Tokoro, M. Yoshikiyo, A. Namai, and S. Ohkoshi, "Phase Separation of ϵ-Fe_2O_3 and $BaFe_{12}O_{19}$ in a Synthesis Combining Reverse-Micelle and Sol-Gel Techniques," *Eur. J. Inorg. Chem.*, vol. 27, no. 22, p. e202400148, Aug. 2024.

[3] P. Narayanan, R. Pramanik, and A. Arockiarajan, "Hard Magnetics and Soft Materials—a synergy," *Smart Mater. Struct.*, vol. 33, no. 4, p. 043001, Apr. 2024.

[4] P. T. Tho *et al.*, "Detailed microwave loss mechanisms for nanocomposites of La-doped $BaFe_{12}O_{19}$ and polyaniline," *Ceram. Int.*, vol. 49, no. 14, pp. 23669–23679, July 2023.

[5] F. Gan *et al.*, "Fabrication of $BaFe_{12}O_{19}/CeO_2$ Composite for Highly Efficient Microwave Absorption," *J. Alloys Compd.*, vol. 897, p. 162964, Mar. 2022.

[6] G. Gultom, M. Rianna, P. Sebayang, and M. Ginting, "The Effect of Mg–Al binary Doped Barium Hexaferrite for Enhanced Microwave Absorption Performance," *Case Stud. Therm. Eng.*, vol. 18, p. 100580, Apr. 2020.

[7] D. S. Winatapura, Deswita, A. A. Wisnu, S. Purwanto, and Y. F. Buys, "Influence of La, Mn, and Zn Substitution on the Structure, Magnetic, and Absorption Properties of M-Type Barium Ferrites," *Key Eng. Mater.*, vol. 855, pp. 145–153, July 2020.

[8] E. Yustanti, A. Noviyanto, M. Ikramullah, Y. A. Marsillam, Y. Taryana, and A. Taufiq, "High-performance Microwave Absorption by Optimizing Hydrothermal Synthesis of $BaFe_{12}$ O_{19} @MnO_2 Core–shell Composites," *RSC Adv.*, vol. 13, no. 39, pp. 27634–27647, 2023.

[9] M. Zahid, S. Siddique, R. Anum, M. F. Shakir, Y. Nawab, and Z. A. Rehan, "M-Type Barium Hexaferrite-Based Nanocomposites for EMI Shielding Application: a Review," *J. Supercond. Nov. Magn.*, vol. 34, no. 4, pp. 1019–1045, Apr. 2021.

[10] R. Chahal *et al.*, "Thermally Conducting Polyaniline Reinforced Expanded Graphite/TiO_2/ $BaFe_{12}O_{19}$ Nanocomposites: Electromagnetic Shielding Performance in Ku-frequency Band," *Ceram. Int.*, vol. 51, no. 15, pp. 20303–20315, June 2025.

[11] I. G. A. P. Adnyana, K. N. Suarbawa, N. P. Y. Nurmalasari, and W. A. Adi, "The Effect of Barium Substitution with Combinations of Rare Earth on Permanent Magnetic Surface Morphology Based on Barium Hexaferrite," *Indones. Phys. Rev.*, vol. 7, no. 2, pp. 185–193, Mar. 2024.

[12] I. Bibi *et al.*, "Effect of Doping on Dielectric and Optical Properties of Barium Hexaferrite: Photocatalytic Performance Under Solar Light Irradiation," *Ceram. Int.*, vol. 47, no. 22, pp. 31518–31526, Nov. 2021.

[13] G. Muhiuddin *et al.*, "Synthesis of Ni Doped Barium Hexaferrite by Microemulsion Route to Enhance the Visible Light-driven Photocatalytic Degradation of Crystal Violet Dye," *Ceram. Int.*, vol. 49, no. 3, pp. 4342–4355, Feb. 2023.

[14] S. Dharani, S. Thanigaivel, S. Rajendran, S. Arunachalam, and W.-H. Chen, "Barium Hexaferrite Nanoparticles Embedded on Graphitic Carbon Nitride for Visible Light Photocatalytic Degradation," *Carbon Lett.*, vol. 35, no. 4, pp. 1599–1610, Aug. 2025.

[15] P. Zhou *et al.*, "Nitrogen-Defect-Modified g-C_3N_4/$BaFe_{12}O_{19}$ S-scheme Heterojunction Photocatalyst with Enhanced Advanced Oxidation Technology Synergistic Photothermal Degradation Ability of Antibiotic: Insights into Performance, Electron Transfer Pathways and Toxicity," *Appl. Catal. B Environ.*, vol. 343, p. 123485, Apr. 2024.

[16] A. Terzić, V. Paunović, and J. Stojanović, "Effect of The Titanium-dioxide Addition on The Structural, Dielectric, and Mechanical Properties of Different Cement-based Mortars with Corundum Aggregate," *Constr. Build. Mater.*, vol. 412, p. 134847, Jan. 2024.

[17] N. Asyiah *et al.*, "Green Synthesis of $TiOaFe_2$ using Aloe Vera for Photodegradation in Sasirangan Waste," *Indones. Phys. Rev.*, vol. 8, no. 1, pp. 85–96, Nov. 2024.

[18] M.-A. Gatou, A. Syrrakou, N. Lagopati, and E. A. Pavlatou, "Photocatalytic TiO2-Based Nanostructures as a Promising Material for Diverse Environmental Applications: A Review," *Reactions*, vol. 5, no. 1, pp. 135–194, Feb. 2024.

[19] R. Mutsak Ahmed and I. Hasan, "A Review on Properties and Applications of TiO_2 and Associated Nanocomposite Materials," *Mater. Today, Proc.*, vol. 81, pp. 1073–1078, 2023.

[20] Z. Peng *et al.*, "Understanding The Ultrahigh Dielectric Permittivity Response in Titanium Dioxide Ceramics," *Ceram. Int.*, vol. 46, no. 2, pp. 2545–2551, Feb. 2020.

[21] T. Wang, Q. Pang, B. Liu, and H. Wang, "Introducing Defects and Crystalline/amorphous Heterostructures on Mesoporous TiO_2 to Realize Broadband Microwave Absorption," *Ceram. Int.*, vol. 51, no. 2, pp. 1643–1653, Jan. 2025.

[22] X. Wu, L. Cao, J. Song, Y. Si, J. Yu, and B. Ding, "Thorn-like Flexible $Ag_2C_2O_4$/TiO_2 Nanofibers as Hierarchical Heterojunction Photocatalysts for Efficient Visible-light-driven Bacteria-killing," *J. Colloid Interface Sci.*, vol. 560, pp. 681–689, Feb. 2020.

[23] M. Humayun, F. Raziq, A. Khan, and W. Luo, "Modification Strategies of TiO_2 for Potential Applications in Photocatalysis: A Critical Review," *Green Chem. Lett. Rev.*, vol. 11, no. 2, pp. 86–102, Apr. 2018.

[24] O. Khemakhem *et al.*, "Magnetic and Photocatalytic Activity of Pure $BaFe_{12}O_{19}$ and $BaFe_{12}O_{19}$-TiO_2 Hexagonal Ferrite Nanocomposites," *J. Supercond. Nov. Magn.*, vol. 35, no. 11, pp. 3371–3378, Nov. 2022.

[25] S. Dudziak, C. Gómez-Polo, J. Karczewski, K. Nikiforow, and A. Zielińska-Jurek, "Insight into (Electro)magnetic Interactions within Facet-Engineered $BaFe_{12}O_{19}$/TiO_2 Magnetic Photocatalysts," *ACS Appl. Mater. Interfaces*, vol. 15, no. 48, pp. 56511–56525, Dec. 2023.

[26] F. S. Razavi, D. Ghanbari, and M. Salavati-Niasari, "Comparative Study on the Role of Noble Metal Nanoparticles (Pt and Pd) on the Photocatalytic Performance of the $BaFe_{12}O_{19}$ /TiO_2 Magnetic Nanocomposite: Green Synthesis, Characterization, and Removal of Organic Dyes under Visible Light," *Ind. Eng. Chem. Res.*, vol. 61, no. 36, pp. 13314–13327, Sept. 2022.

[27] Z. Ebrahimi, K. Hedayati, and D. Ghanbari, "Preparation of Hard Magnetic $BaFe_{12}O_{19}$–TiO_2 Nanocomposites: Applicable for Photo-degradation of Toxic Pollutants," *J. Mater. Sci. Mater. Electron.*, vol. 28, no. 18, pp. 13956–13969, Sept. 2017.

[28] A. V. Trukhanov *et al.*, "Impact of the Heat Treatment Conditions on Crystal Structure, Morphology and Magnetic Properties Evolution in BaM Nanohexaferrites," *J. Alloys Compd.*, vol. 866, p. 158961, June 2021.

[29] E. Handoko *et al.*, "Microwave Absorption Performance of Barium Hexaferrite Multi-nanolayers," *Mater. Express*, vol. 10, no. 8, pp. 1328–1336, Aug. 2020.

[30] N. Hanifah *et al.*, "Defect-engineered Ni-doped *a*-Fe_2O_3@TiO_2/AC nanocomposites for optimized Ka-band radar absorber," *Nano Trends*, vol. 15, p. 100227, Sept. 2026.

[31] X. Wang, B. Wang, S. Wei, Y. Wang, and Y. Liang, "Effect of sintering temperature on the microstructure, magnetic, and microwave absorption properties of M-type barium ferrite nanoparticles prepared by sol–gel method," *J. Mater. Sci. Mater. Electron.*, vol. 34, no. 12, p. 1045, Apr. 2023.

[32] G. K. A. W. Agung, I. B. P. Mardana, and I. G. Arjana, "Synthesis of Magnetite Nanoparticles (Fe_3O_4) Based on Taman River Sand Magnetic Minerals," *Indones. Phys. Rev.*, vol. 7, no. 3, pp. 327–337, June 2024.

[33] E. Puspita, N. Rahmah, M. Naibaho, and R. Ramlan, "Effect of The Composition of TiO_2 Additives on The Physical and Magnetic Properties, Crystal Structure, and Microstructure of $BaFe_{12}O_{19}$ Magnetic Ceramics," *Indones. J. Appl. Phys.*, vol. 13, no. 2, p. 207, Nov. 2023.

[34] M. Me. Barakat, D. E.-S. Bakeer, and A.-H. Sakr, "Structural, Magnetic Properties and Electron Paramagnetic Resonance for $BaFe_{12-x}$ Hg_x O_{19} Hexaferrite Nanoparticles Prepared by Co-Precipitation Method," *J. Taibah Univ. Sci.*, vol. 14, no. 1, pp. 640–652, Jan. 2020.

[35] Y. Noratiqah and N. B. Ibrahim, "Pure polycrystalline barium hexaferrite film prepared without buffer layer, using a sol–gel method," *Appl. Phys. A*, vol. 129, no. 1, p. 1, Jan. 2023.

[36] S. Verma, A. Singh, S. K. Godara, J. Ahmed, S. Alshehri, and M. Singh, "Ca-induced changes in the crystal structure and magnetic properties of barium hexaferrite," *Bull. Mater. Sci.*, vol. 46, no. 4, p. 196, Sept. 2023.

[37] Md. Hossain and S. Ahmed, "Easy and Green Synthesis of TiO_2 (Anatase and Rutile): Estimation of Crystallite Size Using Scherrer Equation, Williamson-Hall plot, Monshi-Scherrer Model, Size-strain Plot, Halder- Wagner Model," *Results Mater.*, vol. 20, p. 100492, Dec. 2023.

[38] K. Polley, R. Kundu, N. Nayak, R. Agarwal, and J. Bera, "Sintering and electromagnetic properties of $BaFe_{12}O_{19}$ ferrite prepared by co-precipitation method," *J. Mater. Sci. Mater. Electron.*, vol. 33, no. 22, pp. 17912–17922, Aug. 2022.

[39] Moatoshi, S. Sarma, and J. P. Borah, "Enhancing structural and magnetic properties of $BaFe_{12}O_{19}$ nanoparticles through co-substitution (Co-Mn): A promising approach for permanent magnet applications," *Phys. Scr.*, vol. 98, no. 12, p. 125966, Nov. 2023.

[40] Himanshi *et al.*, "Insights into the photocatalytic removal of malachite green organic pollutant by highly efficient hard-responsive $Ba_{1-x}Co_xDy_yFe_{12-y}O_{19}$ catalysts," *Sci. Rep.*, vol. 15, no. 1, p. 1225, Jan. 2025.

[41] F. Yamani, ST. U. I. Subadra, N. Mufti, and A. Taufiq, "Preparation of TiO_2/Fe_3O_4/DMSO Ferrofluid as an Antimicrobial Agent," *J. Phys. Conf. Ser.*, vol. 2980, no. 1, p. 012025, Apr. 2025.

[42] S. M. Ismail, Sh. Labib, and S. S. Attallah, "Preparation and Characterization of Nano-Cadmium Ferrite," *J. Ceram.*, vol. 2013, pp. 1–8, Feb. 2013.

[43] N. Ullah, F. A. Jan, S. M. Shah, M. Usman, and M. H. Suliman, "Boosting efficiency of hybrid bulk heterojunction solar cells using organic dyes-grafted Sn-doped ZnS nanohybrid blended with P3HT," *J. Mater. Sci. Mater. Electron.*, vol. 36, no. 25, p. 1591, Sept. 2025.

[44] P. Kumar and A. Kumar, "Review of Morphology and Size-Biased Microwave Absorbing Nanomaterials," *ACS Appl. Nano Mater.*, vol. 8, no. 23, pp. 11731–11762, June 2025.

[45] A. Yu. Mironovich, V. G. Kostishin, H. I. Al-Khafaji, E. S. Savchenko, V. A. Astakhov, and A. I. Ril, "Study of Magnetic and Structural Properties of $BaFe_{12-x}Cu_xO_{19}$ Ferrites Obtained by Hydrothermal Synthesis," *Inorg. Mater. Appl. Res.*, vol. 15, no. 6, pp. 1704–1712, Dec. 2024.

[46] H. Kumar, M. A. Mumtaz, P. Kumari, S. Kumar, A. Manash, and M. I. Khan, "Multifunctional properties of Pr-substituted $BaFe_{12}O_{19}$ hexaferrites: structural, magnetic, optoelectronic, and ferroelectric investigation," *J. Mater. Sci. Mater. Electron.*, vol. 37, no. 12, p. 935, Apr. 2026.

[47] Y. Long *et al.*, "Morphology induced modulation of electromagnetic response in circular BaFe12O19 architectures," *Appl. Phys. A*, vol. 132, no. 8, p. 788, Aug. 2026.

[48] V. K. Rayapu, G. Neeruganti O, R. S. Aley, S. S. Rao Katlagunta, and S. Adiraj, "The effect of lattice strain on magnetic properties of $BaFe_{12}O_{19}$ and $NiFe_2O_4$ thick films prepared via tape casting method," *Phys. B Condens. Matter*, vol. 710, p. 417227, Aug. 2025.

[49] L. Jie *et al.*, "$BaFe_{12}O_{19}$/graphene/polyaniline coatings for flexible fabrics with enhanced microwave absorption," *Text. Res. J.*, vol. 94, no. 3–4, pp. 494–507, Feb. 2024.